Electrochimica Acta 138 (2014) 124–131

Contents lists available at ScienceDirect

Electrochimica Acta

journal homepage: www.elsevier.com/locate/electacta

Formation of barrier-type anodic films on ZE41 magnesium alloy in a fluoride/glycerol electrolyte

J.M. Hernández-López [a], A. Němcová [b], X.L. Zhong [b], H. Liu [b], M.A. Arenas [a], S.J. Haigh [b], M.G. Burke [b], P. Skeldon [b,*], G.E. Thompson [b]

[a] Centro Nacional de Investigaciones Metalúrgicas, CENIM-CSIC, Avda. Gregorio del Amo 8, 28040, Madrid, Spain
[b] School of Materials, The University of Manchester, Manchester M13 9PL, U.K

ARTICLE INFO

Article history:
Received 3 April 2014
Received in revised form 28 May 2014
Accepted 28 May 2014
Available online 4 June 2014

Keywords:
magnesium
anodic oxidation
TEM
SEM
RBS

ABSTRACT

Barrier-type, nanocrystalline anodic films have been formed on a ZE41 magnesium alloy under a constant current density of 5 mA cm^{-2} in a glycerol/fluoride electrolyte, containing 5 vol.% of added water, at 293 K. The films contain magnesium, fluorine and oxygen as the major species, and lower amounts of alloying element species. The films grow at an efficiency of ~0.8 to 0.9, with a formation ratio in the range of ~1.2 to 1.4 nm V^{-1} at the matrix regions and with a ratio of ~1.8 nm V^{-1} at Mg-Zn-RE second phase. At the former regions, rare earth species are enriched at the film surface and zinc is enriched in the alloy. A carbon- and oxygen-rich band within the film suggests that the films grow at the metal/film and film/electrolyte interfaces.

1. Introduction

The formation of barrier-type anodic films has been extensively investigated on the valve metals, especially for aluminium, niobium, tantalum, titanium and zirconium, which have been of particular fundamental and practical interest [1–6]. These studies have shown that oxide films of uniform thickness are formed under a high electric field. The magnitude of the electric field depends upon the structure and composition of the oxide and the rate of film growth, the latter being dependent exponentially on the electric field [7,8]. The films on aluminium, niobium and tantalum are usually amorphous under most conditions of film growth near room temperature. The formation of these films involves migration of metal ions and oxygen ions, with significant contributions to the ionic current of both types of ion, e.g. the transport numbers of Al^{3+}, Nb^{5+} and Ta^{5+} are ~0.40, 0.24 and 0.24 respectively [2]. Further, the outer regions of the oxide films usually contain a low concentration of species derived from the anions of the electrolyte, such as phosphate species for films formed in a phosphate electrolyte [9,10]. In contrast, films formed on zirconium are mainly nanocrystalline and form largely by migration of O^{2-} ions, with a minor contribution from migration of Zr^{4+} ions [11]. Films formed on titanium show an intermediate behaviour, undergoing a transition from amorphous oxide to a mixture of amorphous and crystalline oxide as the film thickens [4].

Due to the relatively low corrosion resistance of magnesium alloys in many environments, anodizing treatments can be applied to provide protection. Several commercial treatments are available, which usually produce relatively thick, porous coatings under conditions of dielectric breakdown [12–14]. Barrier-type films that support high electric fields can also be formed on magnesium [15–22]. Fukada and Matsumoto formed films on AZ91 alloy at low voltage in hydroxide solutions, with and without added silicate [15]; the films consisted mainly of $Mg(OH)_2$. Ono et al examined films formed on magnesium at low voltage in a chromate-fluoride electrolyte [16]. The films were shown to consist of a barrier layer and porous region and were composed of MgF_2 and $Mg_{x+y/2}O_x(OH)_y$. Khaselev et al. [17,18] anodized magnesium and Mg-Al alloys in a hydroxide-phosphate-fluoride solution, with and without additions of aluminate, revealing films composed of MgO and $MgAl_2O_4$. Bonilla et al. employed galvanostatic anodizing of a Mg-W alloy in an alkaline phosphate electrolyte [19]. The composition of the films, which formed at efficiencies of 40 to 50%, was consistent with the presence of mainly hydroxide or oxyhydroxide. Moon and Nam suggested addition of fluoride to sodium hydroxide electrolytes promoted formation of MgF_2 and SnF_4 in films formed on Mg-Sn alloys [20]. Latham et al. employed an ionic liquid for anodizing AZ31 alloy to relatively low voltages, finding

* Corresponding author. Tel.: +44 161 306 4872; fax: +44 161 306 4826.
E-mail address: p.skeldon@manchester.ac.uk (P. Skeldon).

http://dx.doi.org/10.1016/j.electacta.2014.05.147

the anion and cation components of the ionic liquid incorporated into the anodic film [21]. The formation of a film containing MgO, $Mg(OH)_2$ and MgF_2 species has been shown to follow a high-field ionic conduction model [22].

Despite such studies, much less is known of the details of the composition, morphology, structure and growth mechanism of barrier-type anodic films on magnesium compared with anodic films on many other metals. In the present work, employing high-resolution electron microscopy and ion beam analysis, it is shown that barrier-type anodic films of uniform thickness can be formed on a magnesium alloy using a glycerol/fluoride electrolyte. This composition of electrolyte has been used previously to form porous or nanotubular anodic films on titanium and zirconium [23–25]. The films on magnesium are shown to be fluoride-based and to thicken with a formation ratio of ~1.3 nm V^{-1}, which is in the range typical for barrier-type anodic oxides on valve metals. The material selected for the investigation was ZE41 magnesium alloy, a medium strength casting alloy that contains zinc, rare earths and zirconium. The alloy is suited to applications in the aerospace, automotive and electronic industries. The relatively high zinc content of the alloy allowed investigation of the possibility that zinc may be enriched in the alloy as a consequence of anodizing, which has been observed previously in a sputtering-deposited Mg-Zn alloy [26].

2. Experimental

ZE41magnesium alloy (nominal composition in wt%: 3.5-5% Zn, 0.8-1.7% rare earths (RE), 0.4–1.0% Zr, bal. Mg) was supplied by Magnesium Elektron Ltd as a cast slab of 2.5 cm thickness. The slab was cut to provide specimens with dimensions of 2.5 × 2.0 × 1 cm. One face of each specimen, of dimensions 2.5 × 2.0 cm, was then ground on silicon carbide papers and polished to a 1 μm diamond finish. After polishing, the specimens were rinsed in ethanol and dried in a flow of cool air. The specimens were then anodized to selected voltages at 5 mA cm^{-2} in a glycerol-based electrolyte containing 0.35 M ammonium fluoride and 5 vol.% of added water. A perspex cell was used, with a port near the base. Each specimen was clamped against the port, where an O-ring provided a seal with the specimen surface. The working area of the specimen, which was defined by the diameter of the O-ring, was 1.54 cm^2. The cathode was a platinum wire. The current was supplied by a DC constant current source (Metronix Model 6912) power supply. The cell voltage during anodizing was recorded using software based on Labview that was developed in-house. After completion of anodizing, the specimen was removed from the cell, rinsed in de-ionized water and dried as previously.

Scanning electron microscopy (SEM) was used for investigation of the alloy microstructure and the surfaces and cross-sections of the anodic films, employing Zeiss EVO 50 and Zeiss Ultra 55 instruments operated at 15 and 1.5 kV respectively. Cross-sections of anodized specimens were prepared for transmission electron microscopy (TEM) using a Quanta 3D dual beam focused ion beam (FIB) instrument with the OmniProbe in-situ lift-out technique. Specimens were coated with platinum to prevent damage during ion beam bombardment. The FIB was operated using a 30 kV ion beam, with currents of 3-7 nA for rough cutting and 0.1 nA for final cleaning. The resulting thin section was welded onto the wall of a copper TEM half grid. High resolution TEM imaging and electron diffraction was performed in an FEI Tecnai F30 (scanning) transmission electron microscope (S)TEM instrument operated at 300 kV and equipped with an Oxford Instrument X-Max80 energy-dispersive X-ray spectroscopy (EDXS) system. High angle annular dark field (HAADF) STEM imaging was performed using a probe aberration corrected FEI Titan G2 80-200 ChemiSTEM™ (S)TEM instrument, operated at 80 kV, with a convergence angle of 18 mrad and a HAADF inner angle of 54 mrad. EDXS was performed using the Titan's four windowless silicon drift detector EDXS system with a total collection solid angle of 0.7 srad.

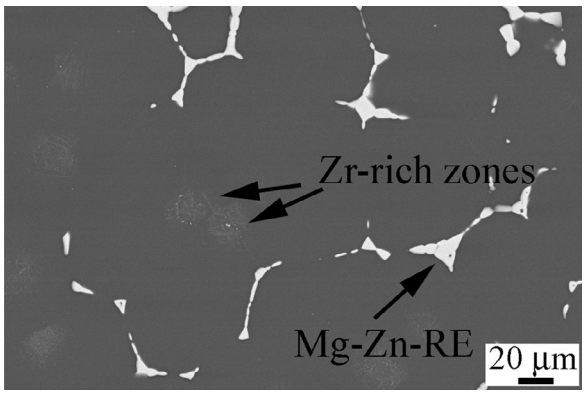

Fig. 1. Backscattered electron scanning electron microscope image showing the surface of the mechanically polished ZE41 alloy.

The compositions of anodic films were investigated by Rutherford backscattering spectroscopy (RBS) employing 3.045 MeV $^4He^+$ ions (making use of the resonance in the $^{16}O(\alpha,\alpha_0)^{16}O$ reaction) supplied by the van de Graff generator at the Centro de Micro-Análisis de Materiales (CMAM), Madrid. The incident ion beam was normal to the specimen surface, with scattered ions detected at 165°. The data were interpreted using SIMNRA software.

Elemental depth profiling of specimens was performed by glow discharge optical emission spectroscopy (GDOES), using a GD-Profiler 2 instrument (Horiba Jobin Yvon). The measurements were made in the continuous mode, using a copper anode of 4 mm diameter, with an argon pressure of 635 Pa, a power of 35 W and a flush time 30 s. Light emitted by sputtered species was monitored with a sampling interval of 0.01 s at wavelengths (nm) of 383.829, 481.053, 417.732, 339.198 and 130.217 for magnesium, zinc, neodymium, zirconium and oxygen respectively.

3. Results

3.1. Alloy microstructure

Fig. 1 shows a backscattered electron scanning electron microscope image of the mechanically-polished surface of the ZE41 alloy before anodizing. The main features of interest with regard to the anodizing behaviour are the alloy matrix and Mg-Zn-RE phase at the grain boundaries, the latter being evident as light regions in the backscattered electron image. EDX analysis indicated that the RE consisted mainly of neodymium. It is later shown that a significantly thicker anodic film is formed above the Mg-Zn-Re regions than above the matrix. Fine zirconium-rich particles are also present in localized regions of the matrix. In the literature, the grain boundary phase has been assigned to Mg_7Zn_3RE or $Mg_{12}RE$ (RE = rare earth) and the fine zirconium-rich particles to Zr_4Zn or Zn_2Zr_3 [27–31].

3.2. Cell voltage-time behaviour

Fig. 2 shows the cell voltage during anodizing of the alloy. After a surge to ~47 V, which is mainly due to the resistance of the electrolyte and of any pre-existing oxide/hydroxide film on the alloy surface, three regions are evident of approximate gradients ~4.7 ± 0.2, ~2.3 ± 0.2 and ~4.4 ± 0.2 V s^{-1} lasting for ~5, 15 and 85 s respectively, with intermediate short periods of transition. Thereafter, the voltage fluctuates when dielectric breakdown begins.

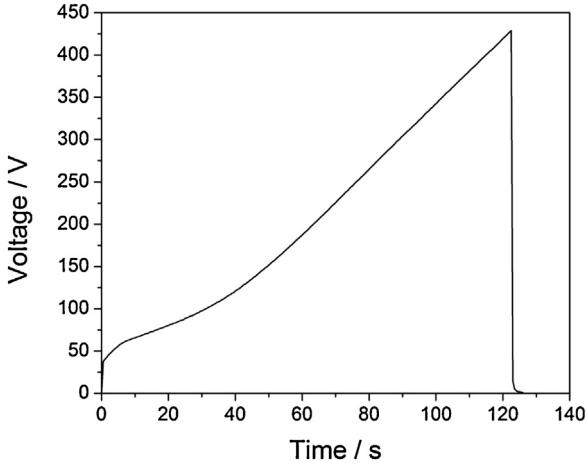

Fig. 2. Dependence of the cell voltage on anodizing time for ZE41 magnesium alloy in 0.35 M fluoride/glycerol electrolyte containing 5 vol.% of added water.

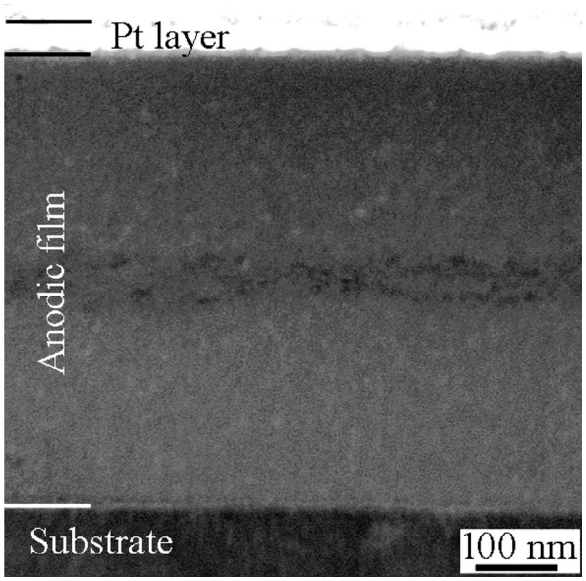

Fig. 3. HAADF scanning transmission electron microscope image showing a cross section extracted through the anodic film formed at a matrix region of the ZE41 alloy anodized to 440 V in 0.35 M fluoride/glycerol electrolyte containing 5 vol.% of added water.

Films for subsequent investigation were formed to 110 and 440 V, i.e. to the end of the second and third regions. The voltage increments due to film growth were ~63 and 393 V; the charges passed in the cell were 0.103 and 0.548 C cm^{-2} respectively.

3.3. Transmission electron microscopy

Fig. 3 presents a HAADF scanning transmission electron microscope image showing the extracted cross-section after anodizing to 440 V. The region of the section corresponds to the anodic film above the alloy matrix. It is later shown that the film is modified above regions of Mg-Zn-RE second phase. The protective platinum layer applied during sample preparation is visible as the brightest band at the top of the image. An anodic film of thickness ~570 ± 10 nm, which has relatively flat alloy/film and film/electrolyte interfaces, is revealed beneath the platinum layer. The formation ratio is ~1.45 nm V^{-1}. A darker band, ~50 nm thick, lies close to the middle of the film. A high-resolution TEM image of the anodized film is shown in Fig. 4(a). Lattice fringes indicate

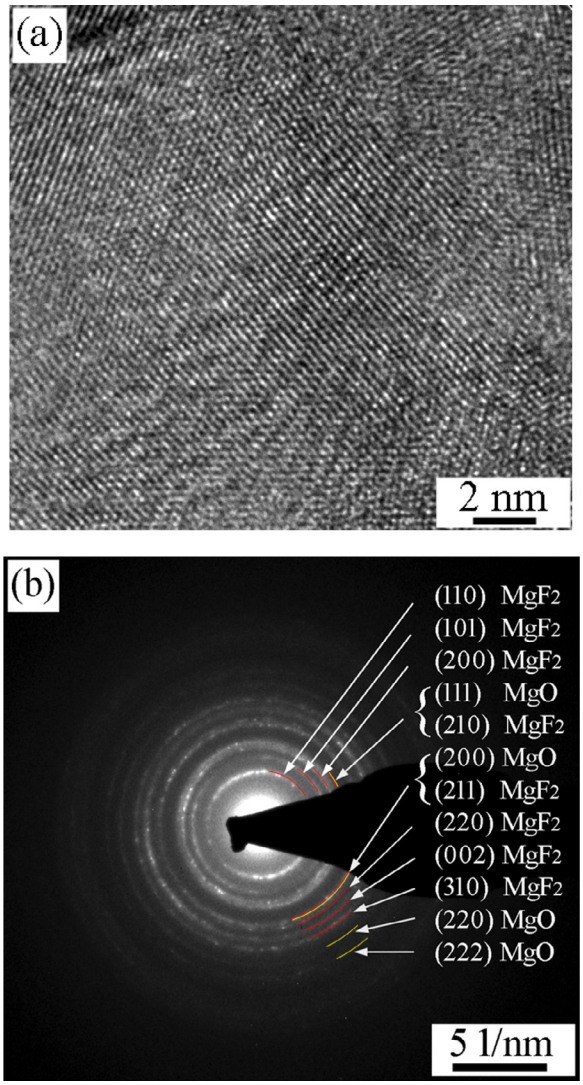

Fig. 4. (a) High resolution transmission electron micrograph of the anodic film formed at a matrix region of the ZE41 alloy anodized to 440 V in 0.35 M fluoride/glycerol electrolyte containing 5 vol.% of added water. (b) Electron diffraction pattern of the film.

a nanocrystalline structure, which was evident throughout the film thickness. The nanocrystalline structure was confirmed by the electron diffraction ring pattern shown in Fig. 4(b), in which lattice spacings could be identified that are consistent with MgF_2 and MgO.

Fig. 5 shows the results of EDXS spectrum imaging of a second film cross-section with elemental maps extracted for magnesium, fluorine, oxygen, carbon and zinc. Magnesium, fluorine and oxygen species are distributed relatively uniformly throughout the film thickness, with the exception of a central band, of width ≤ 20 nm, that is depleted in magnesium and fluorine but enriched in oxygen and carbon. A low level of zinc and neodymium was found in EDX spectra obtained both from the alloy and the anodic film. However, the small signals could be due to stray scattering within surrounding material. The map for neodymium is not shown owing to the low signals. However, the map for zinc is displayed due to the clear presence of an enrichment of zinc beneath the anodic film that is considered later. The maps indicate a film thickness of 456 ± 10 nm, corresponding to a nm V^{-1} ratio of 1.16 nm V^{-1}. The thickness determined from Fig. 5 is lower than that determined from Fig. 3, probably due to parallax as a result of the FIB section being slightly tilted with respect to the incident electron beam

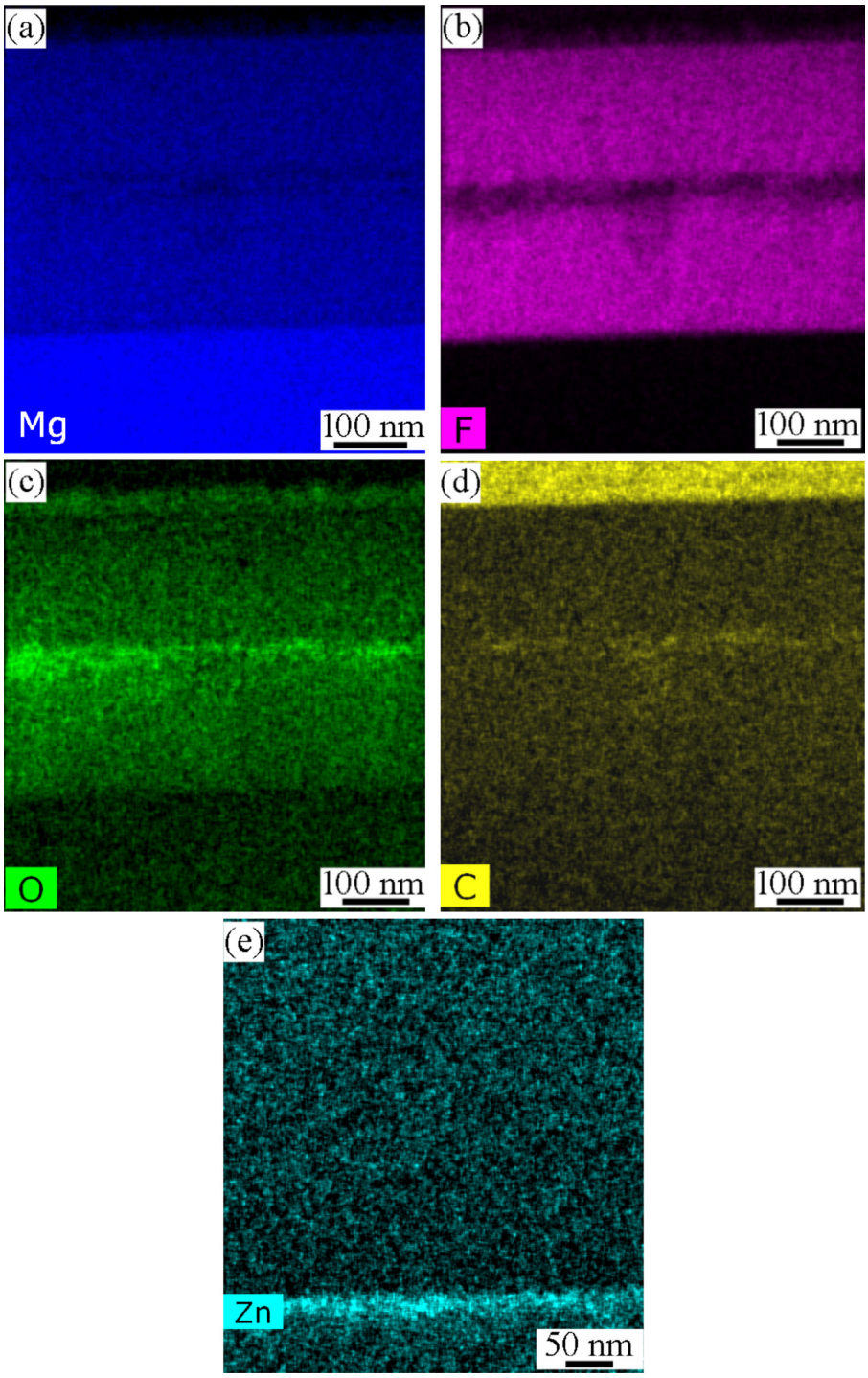

Fig. 5. Energy-dispersive X-ray spectrum imaging of ZE41 magnesium alloy following anodizing to 440 V in 0.35 M fluoride/glycerol electrolyte containing 5 vol.% of added water. Elemental maps have been extracted for (a) Mg; (b) F; (c) O, (d) C; (e) Zn.

and/or differing angles of milling during preparation of the two sections by FIB.

The central band, which is presumed to consist mainly of carbon-contaminated oxide/hydroxide, is possibly formed on the alloy either before the commencement of anodizing, i.e. during polishing, subsequent exposure to air and following immersion in the electrolyte, or just at the start of anodizing, i.e. before establishment of the main anodic film material, with carbon being due to incorporated glycerol. Based on this assumption, the location of the band suggests that the film has grown by inward migration of anion species, forming the inner film region, and the outward migration of cation species, forming the outer film region. The ions may migrate across the band through paths that isolate islands of residual oxide/hydroxide, which then remain as immobile constituents of the film. The paths may form if the band is porous or if a high electric field is required for ionic transport within the initial material compared with the subsequently formed film material [2,32,33]. However, with respect to the latter process, such penetration was not observed in anodizing of zirconium covered by a thin layer of aluminium when nanocrystalline anodic zirconia was

formed beneath amorphous anodic alumina [34]. Counter migration of anion and cation species is typical of amorphous anodic oxide films, whereas nanocrystalline oxides usually form mainly by inward migration of oxygen species [2,11]. Counter migration of anions and cations may occur in the present films if the nanocrystalline structure transforms to an amorphous structure under the electric field imposed by anodizing. However, it is also possible that ionic transport mechanism differs in the fluoride-based films from that in the oxide-based films, with anions and cations migrating at crystallite boundaries.

Fig. 5(e) reveals that an enrichment of zinc is present in the alloy matrix immediately beneath the anodic film, with the thickness of the enriched layer being ~10 nm. Zinc in solid solution in the alloy is expected to enrich in a thin layer of the alloy immediately beneath the anodic film before it can be oxidized and incorporated into the anodic film [26]. Enrichment of alloying elements in solid solution has been observed in dilute aluminium and magnesium alloys. It occurs when the Gibbs free energy per equivalent for formation of the alloying element oxide is less negative than that for formation of Al_2O_3 or MgO [26,35]. Since the present alloy was initially mechanically polished, only a small enrichment exists at the start of anodizing beneath the relatively thin oxide/hydroxide film on the surface of the mechanically-polished alloy. The estimated thickness of the film from later results of RBS was 10 nm. If a similar thickness of alloy was oxidized to form the film, an enrichment of zinc of 0.5 to 1×10^{14} atoms cm^{-2} is predicted, based on a level of zinc in solid solution between 1 and 2 at.%, which are toward the upper limits on the concentration of zinc in solid solution. In comparison, a previous study of a Mg-1.4at.%Zn alloy revealed an enrichment of 5.2×10^{15} zinc atoms cm^{-2} beneath a relatively thick anodic film. The initial enrichment of the present alloy is therefore probably insufficient for oxidation of the zinc to take place in the early stages of anodizing. However, further anodizing may enhance the enrichment to the critical level that allows the enriched zinc to be oxidized. Other alloying elements in the ZE41 alloy are either less noble than magnesium or of a similar nobility. Hence, no major changes in the alloy are expected due to the presence of these elements in solid solution.

3.4. Scanning electron microscopy

Fig. 6(a,b) shows high magnification secondary electron scanning electron microscope images of the surfaces of the specimens anodized to 110 and 440 V respectively. The surface at the lower voltage, presented in Fig. 6(a)), is of a less uniform appearance, due to the influence of the alloy microstructure on the formation of a relatively thin anodic film, later estimated by RBS to be ~73 nm. Occasional, small cavities are possibly regions where anodic film material has detached. The surface corresponding to the high voltage appears smoother, with finer surface features of up to a few tens of nanometres in size, compared with up to several hundred nanometres for anodizing at the lower voltage. The linear feature in Fig. 6(b) is the result of the film being modified at the boundary of a Mg-Zn-RE second phase particle.

Fig. 7 shows scanning electron microscope backscattered electron images of cross-sectional samples prepared by cutting a specimen anodized to 440 V with a diamond knife. The specimen was first coated with a thin layer of platinum, which is visible in these backscattered electron images as the bright band on the top surface of the film. The uniformity of the platinum layer indicates that the film was not damaged by the sectioning procedure. As shown in Fig. 7(a) the film thickness above the matrix regions was determined as 505 ± 15 nm, in reasonable agreement with that shown previously in Figs. 3 and 5, indicating a formation ratio of 1.28 nm V^{-1}. The cross section also reveals occasional small second phase particles within the matrix, which appear as bright regions

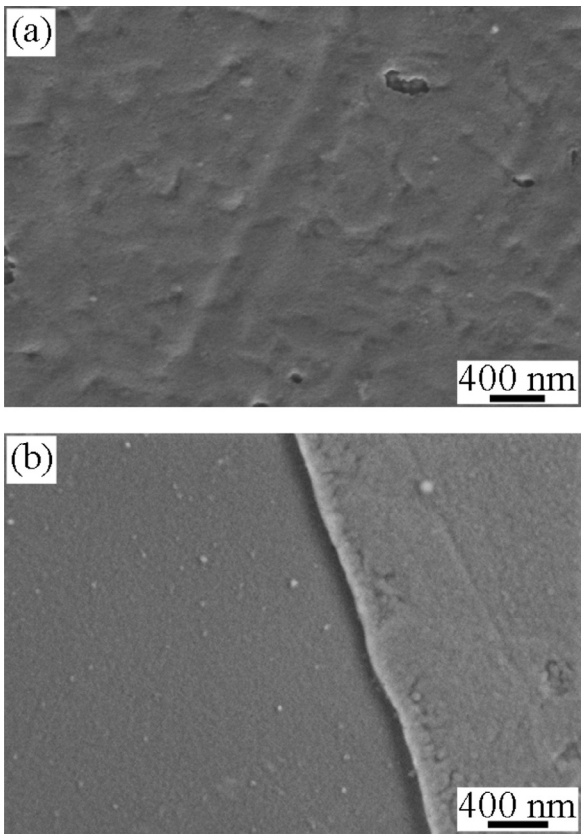

Fig. 6. Secondary electron scanning electron microscope images of the surface of ZE41 magnesium alloy following anodizing to (a) 110 V and (b) 440 V in 0.35 M fluoride/glycerol electrolyte containing 5 vol.% of added water.

in the backscattered electron image and were found to contain zinc and zirconium by EDX analysis. In contrast, Fig. 7(b) shows that above the large Mg-Zn-RE phase regions the film thickness is increased to 715 ± 10 nm, corresponding to a formation ratio of ~1.82 nm V^{-1}. The film appears brighter above the second phase regions than above the matrix indicating the presence of relatively heavy alloying element species, likely to be mainly Nd and/or Zn. A darker band is again observable within the anodized film but much closer to the surface at a depth of 87 ± 10 nm compared with 252 ± 13 nm above the matrix regions. The former depth corresponds to the band being located at ~13% of the film thickness above the second phase regions compared to ~50% of the film thickness above the matrix regions. With the exception of the darker band already discussed, no significant variations in contrast occur through the film thickness suggesting that the film is of relatively

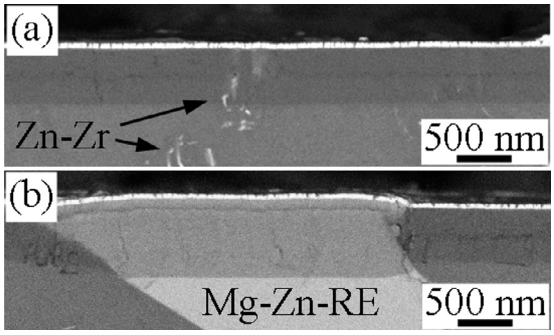

Fig. 7. Backscattered electron scanning electron microscope images of cross-sections of the ZE41 magnesium alloy following anodizing to 440 V in 0.35 M fluoride/glycerol electrolyte containing 5 vol.% of added water.

uniform composition. The dark lines in the sections, orientated approximately normal to the substrate, are fracture features caused by the cutting procedure. The damage appears to be greater in the vicinity of the large second phase particles, which are probably harder than the matrix. The sectioning also caused the film region above the darker band feature to detach at some locations, which may explain the cavities observed in SEM image of the film surface (Fig. 6(a)). Such localized detachment may be initiated at boundaries between the matrix and the second phase owing to stresses generated by the differing oxidation rates and film thicknesses at the two regions.

The large Mg-Zn-RE phase modifies the thickness of the anodic film due to the significant presence of alloying element species that are incorporated into the anodic film. The band of oxide/hydroxide is located closer to the surface than in the film at the matrix regions, which may be due differences in the composition of the film and the transport numbers of film species at the two regions. It is also possible that ejection of species at the film/electrolyte interface, or dissolution of the film, may have reduced the thickness of the outer layer. Smaller zirconium-zinc-rich second phase particles appear to be oxidized, with cation species being presents within the inner and outer regions of the film.

3.5. Ion beam analysis

Fig. 8 shows the RBS spectra for the ZE41 alloy before anodizing and after anodizing to either 110 or 440 V. The alloy initially shows the presence of an oxide/hydroxide film that contains 5.1×10^{16} oxygen atoms cm^{-2}. The oxygen content suggests a ~10 nm thick film, assuming that the main constituent is MgO and/or $Mg(OH)_2$. After anodizing to 110 V, the oxygen and fluorine contents of the film were ~ 1.37×10^{17} and 2.89×10^{17} atoms cm^{-2}, with an atomic ratio of oxygen to fluorine of ~0.48. The estimated film thickness is ~73 nm, based on the average concentrations of fluorine and oxygen in MgF_2 and MgO (6.0875×10^{22} and 5.347×10^{22} atoms cm^{-3}). The film thickness corresponds to a formation ratio of 1.16 nm V^{-1}. Following anodizing to 440 V, the fluorine and oxygen contents increased to 20.677×10^{17} and 3.791×10^{17} atoms cm^{-2}, corresponding to an atomic ratio of oxygen to fluorine of ~0.18. The estimated film thickness of 411 nm suggests a formation ratio of 1.05 nm V^{-1}. The formation ratios determined from RBS are in reasonable agreement with the results of electron microscopy, given the uncertainty in the atomic densities of the films and the stopping power of the films for $^4He^+$ ions. The increased atomic ratio of oxygen to fluorine in the film formed to 110 V can be explained by the greater contribution of the initial carbon-contaminated, oxide/hydroxide material to the film composition.

The yields from zinc, zirconium and rare earth species in the anodic films partially overlap, preventing an accurate measure of their concentrations. However, for the thicker film, the yield from the neodymium is free of overlap above channel 920, which corresponds to the outer ~60% of the film thickness. The data clearly show an enrichment of RE species, presumed to be mainly neodymium species, in the outer ≤15% of the film thickness. The RBS analysis indicated an atomic ratio of neodymium to magnesium in the film region beneath the neodymium-rich surface region of ~0.0054, compared with 0.0067 for the bulk alloy, with the ratio in the enriched region near the film surface increasing by a factor of ~3. The charges of the cation species, presumed to consist of Mg^{2+}, Nd^{3+}, Zn^{2+} and Zr^{4+} ions, in the films formed to 110 and 440 V were 0.0853 and 0.444 C cm^{-2} respectively. Since the percentages of neodymium, zinc and zirconium species in the films are relatively low, uncertainties in their concentrations have only a minor effect on the estimations of the charges of the cations. The charge of the anions, presumed to be F^- and O^{2-} ions, were 0.0901 and 0.453 C cm^{-2}, in reasonable agreement with the charges of the

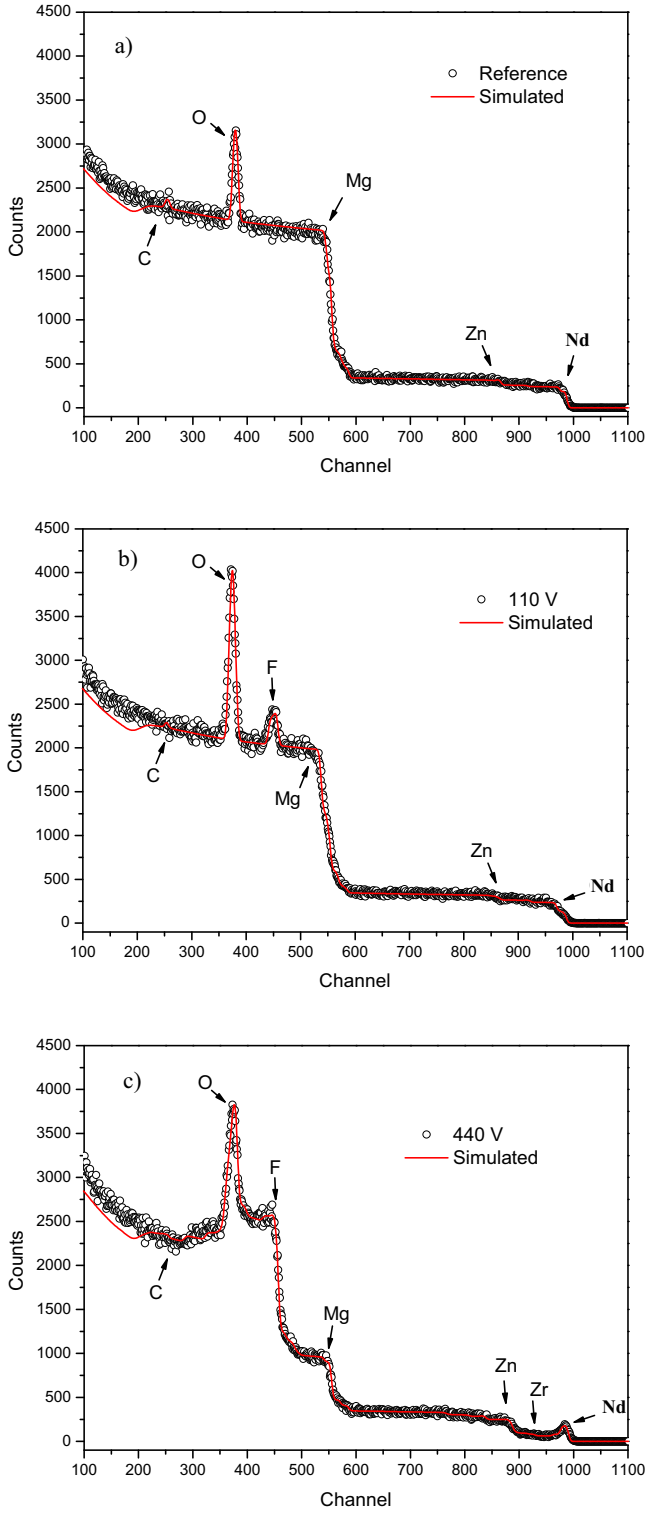

Fig. 8. Experimental and simulated (solid line) RBS spectra for ZE41 magnesium alloy: (a) before anodizing; following anodizing to (b) 110 and (c) 440 V in 0.35 M fluoride/glycerol electrolyte containing 5 vol.% of added water.

cations. The ratios of the average of the cation and anion charges to the charges used to form the films indicate efficiencies of film growth of ~0.85 and ~0.82 for anodizing at 110 and 440 V respectively. The efficiency of anodizing suggests (i) the presence of a side reaction, such as oxygen generation, (ii) loss of film species to the electrolyte, by ejection of ions from the film, dissolution of the film or detachment of film or (iii) initial dissolution of the alloy, which is

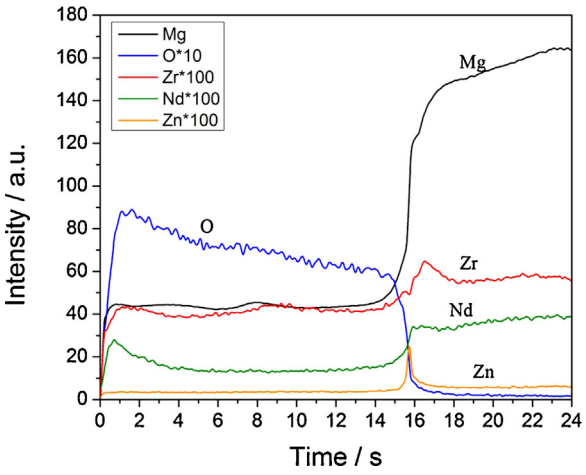

Fig. 9. GDOES elemental depth profiles for ZE41 magnesium alloy following anodizing to 440 V in 0.35 M fluoride/glycerol electrolyte containing 5 vol.% of added water.

terminated by the growth of the anodic film. Other work, to be published as part of a subsequent study, has indicated that the surface treatment of the alloy has an important influence on the efficiency.

3.6. Glow discharge optical emission spectroscopy

Fig. 9 shows the dependence of the optical emissions from magnesium, oxygen, zirconium, neodymium and zinc species on the time of sputtering for a specimen anodized to 440 V. It was not possible to detect fluorine under the present conditions of analysis, which used argon as the sputtering gas. The magnesium, oxygen, zirconium and neodymium species are present throughout the thickness of the anodic film, with neodymium species appearing to be enriched near the film surface. The neodymium-rich region occupied roughly 10% of the time to sputter through the whole of the film, which is reasonably consistent with the thickness of the neodymium-rich region indicated by RBS. The enrichment of neodymium was not detected by EDXS analysis owing to the relatively low concentration of neodymium in the film. In amorphous oxides, the migration of cation species derived from alloying elements of the substrate often correlates with the strength of their bonding with oxygen ions [36,37]. Thus, alloying element species that have a metal-oxygen single bond energy lower than that of the host oxide migrate faster than the cations of the host oxide and vice versa. Generally Nd^{3+} ions appear to migrate faster than Mg^{2+} ions in the present films resulting in the enrichment of the neodymium near the film surface. Oxygen appeared to be increased toward the film surface. The signal from zinc revealed a sharp peak at the anodic film/alloy interface, confirming the enrichment of zinc evident from TEM. Zirconium also reveals a peak near the film/alloy interface. The peak is much broader than that for zinc and is located more deeply in the alloy. It is not possible to identify the precise reason for the peak, although it is speculatively suggested that it is related to the oxidation of the second phase, where the film is thicker than at the matrix regions. The concentration of zinc in the film was below detection limits.

3.7. Mechanism of film growth

Fig. 10 shows a schematic diagram of the suggested growth mechanism of the anodic film on the matrix regions of the alloy. The diagram is based on the findings for the film formed to 440 V. For the purpose of constructing the diagram, the growth of the film has been assumed to occur at an efficiency of 0.82, with a formation ratio of 1.3 nm V^{-1}. The reduced efficiency is assumed to be due to a side reaction. Hence, only 0.82 of the charge passed is used in oxidizing the matrix, which is composed mainly of magnesium. Thus, the film thickness is shown as 1.56 times the thickness of the layer of oxidized matrix. A lower thickness ratio of 1.28 would apply should the reduced efficiency be due to dissolution of metal species. The ratios and the location of the carbon- and oxygen-rich marker layer suggest a cation transport number between 0.5 to 0.6. The estimate neglects the influence of the film growth above the second phase on the current density at the matrix regions. However, this is expected to have a minor effect given the relatively small proportion of the anodized area occupied by second phase. Fig. 10(a) shows the initial condition of the alloy, with a carbon- and oxygen-rich layer on the surface. For present purposes, the layer is assumed to act as an immobile marker within the subsequently formed anodic film, shown in Fig. 10(b). The film grows by outward migration of Mg^{2+} ions and inward migration of F^- and O^{2-} ions. The diagram does not include the migration of alloying element species, which are minor components of the film above the matrix. Further, barrier anodic films inevitably contain defects associated with the effects of stresses in the film and with the differences in film formation above the various microstructural regions of the alloy [38]. The defects are significant in determining the corrosion protection of the alloy, since pitting can initiate at such locations. The corrosion protection provided by the present type of film will be examined in the future studies of the authors.

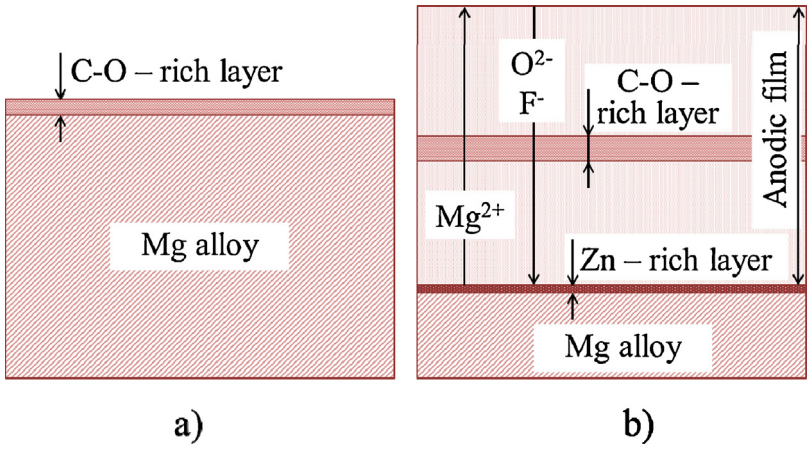

Fig. 10. Schematic diagrams of the growth of the anodic film on the matrix regions of the ZE41 magnesium alloy. (a) Initial alloy surface, with a carbon- and oxygen-rich layer that acts as a marker during subsequent growth of the anodic film. (b) Formation of the anodic film by outward migration of Mg^{2+} ions and inward migration of F^- and O^{2-} ions. The marker is located near the centre of the anodic film.

4. Conclusions

1. Barrier-type anodic films can be formed on ZE41 magnesium alloy under a constant current density of 5 mA cm^{-2} in a glycerol electrolyte containing 0.35 mol dm^{-3} NH_4F and 5 vol.% of added water at 293 K. The efficiency of film growth is in the range 0.8 to 0.9.
2. The film thickness and composition differ between the matrix and second phase regions of the alloy, with a significantly thicker film forming over the large Mg-Zn-RE second phase.
3. The main components of the film at the matrix regions of the alloy are magnesium, fluorine and oxygen species; the atomic ratio of oxygen to fluorine is ~0.2 for a film formed to 440 V.
4. The film at the matrix regions is mainly nanocrystalline and contains MgF_2 and MgO. The formation ratio is in the range ~1.2 to 1.4 nm V^{-1}, compared with ~1.8 nm V^{-1} at the Mg-Zn-RE second phase.
5. Alloying element species are present in all regions of the films formed. The rare-earth species in the film formed above the matrix regions are enriched in a relatively thin region adjacent to the film surface. Zinc is enriched in the alloy in a thin layer immediately beneath the anodic film.
6. The presence of a carbon- and oxygen-rich band within the film suggests that the film forms by migration of cation species outward and anion species inward. The band is close to the middle of the film at matrix regions, but closer to the film surface at the Mg-Zn-RE second phase.

Acknowledgements

The authors are grateful to the Engineering and Physical Sciences Research Council (U.K) for the support of the LATEST2 Programme Grant. The FEI Titan G2 80-200 S/TEM is funded with support from HM Government (UK) and is associated with research capability of the Nuclear Advanced Manufacturing Research Centre. Juan Manuel Hernández López acknowledges CSIC for funding this work under the grant Short Term's JAEPre-2012. Part of this work was supported by Spanish Ministry of Science and Innovation (Consolider-Ingenio 2010-CSD-2008-0023-FUNCOAT).

References

[1] F. Brown, W.D. Mackintosh, The use of Rutherford backscattering to study the behavior of ion-implanted atoms during anodic oxidation of aluminum: Ar, Kr, Xe, K, Rb, Cs, Cl, Br, and I, J. Electrochem. Soc 120 (1973) 1096–1102.
[2] J.P.S. Pringle, The anodic oxidation of superimposed metallic layers: theory, Electrochim. Acta. 25 (1980) 1423–1437.
[3] J.P.S. Pringle, Transport numbers of metal and oxygen during the anodic oxidation of tantalum, J. Electrochem. Soc. 120 (1973) 398–407.
[4] H. Habazaki, M. Hozumi, H. Konno, K. Shimizu, P. Skeldon, G.C. Thompson, Crystallization of anodic titania on titanium and its alloys, Corros. Sci. 45 (2003) 2063–2073.
[5] N. Khalil, A. Bowen, J.S.L. Leach, The anodic oxidation of valve metals—II. The influence of the anodizing conditions on the transport processes during the anodic oxidation of zirconium, Electrochim. Acta 33 (1988) 1721–1727.
[6] C. Ortega, J. Siejka, A study by nuclear microanalysis and ^{18}O tracing of the growth of anodic oxide films on zirconium: II. Oxide Growth Mechanism, J. Electrochem. Soc. 129 (1982) 1905–1917.
[7] A.C. Harkness, L. Young, High resistance anodic oxide films on aluminium, Can. J. Chem. 44 (1966) 2409–2413.
[8] Y.M. Li, L. Young, Anodic oxide films on tantalum: anomalies in steady–state and stepped field ionic conduction and incorporation of electrolyte species, Proc. Royal Soc. A 454 (1998) 239–246.
[9] J.J. Randall, W.J. Bernard, R.R. Wilkinson, A radiotracer study of the composition and properties of anodic oxide films on tantalum and niobium, Electrochim. Acta 10 (1965) 183–201.
[10] H. Takahashi, K. Fujimoto, H. Konno, M. Nagayama, Distribution of anions and protons in oxide films formed anodically on aluminum in a phosphate solution, J. Electrochem. Soc. 131 (1984) 1856–1861.
[11] J.A. Davies, B. Domeij, J.P.S. Pringle, F. Brown, The migration of metal and oxygen during anodic film formation, J. Electrochem. Soc. 112 (1965) 675–680.
[12] J.E. Gray, B. Luan, Protective coatings on magnesium and its alloys — a critical review, J. Alloys Comp. 336 (2002) 88–113.
[13] K. Murakami, M. Hino, M. Hiramatsu, K. Nakai, S. Kobayashi, A. Saijo, T. Kanadani, Corrosion protection of AZ91D magnesium alloy by anodization using phosphate electrolyte, Mater. Trans. 48 (2007) 3101–3108.
[14] A.L. Yerokhin, A. Shatrov, V. Samsonov, P. Shashkov, A. Leyland, A. Matthews, Fatigue properties of Keronite® coatings on a magnesium alloy, Surf. Coat. Technol. 182 (2004) 78–84.
[15] H. Fukada, Y. Matsumoto, Effects of Na_2SiO_3 on anodization of Mg-Al-Zn alloy in 3 M KOH solution, Corros. Sci. 46 (2004) 2135–2142.
[16] S. Ono, K. Asami, T. Osaka, N. Masuko, Structure of anodic films formed on magnesium, J. Electrochem. Soc. 143 (1996) L62–L63.
[17] O. Khaselev, J. Yahalom, The anodic behaviour of Mg-Al alloys in KOH-aluminate solutions, Corros. Sci. 40 (1998) 1149–1160.
[18] J. Yahalom, O. Khaselev, Constant voltage anodizing of Mg-Al alloys in KOH-$Al(OH)_3$ solutions, J. Electrochem. Soc. 145 (1998) 190–193.
[19] F. Bonilla, P. Skeldon, G.E. Thompson, H. Habazaki, K. Shimizu, C. John, K. Stevens, Formation of anodic films on magnesium alloys in an alkaline phosphate electrolyte, J. Electrochem. Soc. 149 (2002) B4–B13.
[20] S. Moon, Y. Nam, Anodic oxidation of Mg-Sn alloys in alkaline solutions, Corros. Sci. 65 (2012) 494–501.
[21] J.-A. Latham, P.C. Howlett, D.R. MacFarlane, A. Somers, M. Forsyth, Anodizing AZ31 in a phosphonium ionic liquid:corrosion protection through composite film dissolution, J. Electrochem. Soc. 159 (2012) C539–C545.
[22] M. Santamaria, F. Di Quarto, S. Zanna, P. Marcus, The influence of surface treatment on the anodizing of magnesium in alkaline solution, Electrochim. Acta 56 (2011) 10533–10542.
[23] F. Muratore, A. Baron-Wiecheć, T. Hashimoto, A. Gholinia, H. Habazaki, P. Skeldon, G.E. Thompson, Porous anodic film growth on a Zr-W alloy, Electrochem. Solid-State Lett. 15 (2012) C8–C11.
[24] J.M. Macak, H. Tsuchiya, L. Taveira, S. Aldabergerova, P. Schmuki, Smooth anodic nanotubes, Angewandte Chemie 44 (2005) 7463–7465.
[25] A. Valota, D.J. LeClere, P. Skeldon, M. Curioni, T. Hashimoto, G.E. Thompson, S. Berger, J. Kunze, P. Schmuki, Influence of water content on nanotubular anodic titania formed in fluoride/glycerol electrolytes, Electrochim. Acta 54 (2009) 4321–4327.
[26] M. Abulsain, A. Berkani, F.A. Bonilla, Y. Liu, P. Skeldon, G.E. Thompson, P. Bailey, T.C.Q. Noakes, K. Shimizu, H. Habazaki, Anodic oxidation of Mg-Cu and Mg-Zn alloys and enrichment of alloying elements, Electrochim. Acta 49 (2004) 899–904.
[27] W.C. Neil, M. Forsyth, P.C. Howlett, C.R. Hutchinson, B.R.W. Hinton, Corrosion of magnesium alloy ZE41–The role of microstructural features, Corros. Sci. 51 (2009) 387–394.
[28] W.C. Neil, M. Forsyth, P.C. Howlett, C.R. Hutchinson, B.R.W. Hinton, Corrosion of heat treated magnesium alloy ZE41, Corros. Sci. 53 (2011) 3299–3308.
[29] N. Dinodi, A. Nityananda Shetty, Electrochemical investigations on the corrosion behaviour of magnesium alloy ZE41 in a combined medium of chloride and sulphate, J. Mag. Alloys 1 (2013) 201–209.
[30] M.C. Zhao, M. Liu, G.L. Song, A. Atrens, Influence of pH and chloride ion concentration on the corrosion of Mg alloy ZE41, Corros. Sci. 50 (2008) 3168–3178.
[31] R. Ding, C. Chung, Y. Chiu, P. Lyon, Effect of ECAP on microstructure and mechanical properties of ZE41 magnesium alloy, Mater. Sci. Eng. A 527 (2010) 3777–3784.
[32] J.P.S. Pringle, Transport numbers of metal and oxygen during the anodic oxidation of tantalum, J. Electrochem. Soc. 120 (1973) 1423–1437.
[33] L. Iglesias-Rubianes, P. Skeldon, G.E. Thompson, H. Habazaki, K. Shimizu, Ionic transport in anodically oxidized Al/W layers, J. Electrochem. Soc. 149 (2002) B23–B26.
[34] K. Shimizu, K. Kobayashi, P. Skeldon, G.E. Thompson, G.C. Wood, Anodic oxidation of zirconium covered with a thin layer of aluminium, Thin Solid Films 295 (1997) 156–161.
[35] H. Habazaki, K. Shimizu, P. Skeldon, G.E. Thompson, G.C. Wood, X. Zhou, Effects of alloying elements in anodizing of aluminium alloys, Trans. Inst. Met. Finishing 75 (1997) 18–23.
[36] H. Habazaki, X. Zhou, K. Shimizu, P. Skeldon, G.E. Thompson, G.C. Wood, Incorporation and mobility of zinc ions in anodic alumina films, Thin Solid Films 292 (1997) 150–155.
[37] H. Habazaki, K. Shimizu, S. Nagata, P. Skeldon, G.E. Thompson, G.C. Wood, Ionic mobility in amorphous titania, J. Electrochem. Soc. 149 (2002) B70–B74.
[38] G.E. Thompson, K. Shimizu, G.C. Wood, Observation of flaws in anodic films on aluminium, Nature 286 (1980) 471–472.